Journal of King Saud University – Science 34 (2022) 101682

Contents lists available at ScienceDirect

Journal of King Saud University – Science

journal homepage: www.sciencedirect.com

Original article

Effects of bismuth and bismuth-copper substitutions on structure, morphology, and magnetic properties of sol-gel derived barium hexaferrites

Komkrich Chokprasombat [a], Abdulmumeen Lohmaah [a], Supree Pinitsoontorn [b], Chitnarong Sirisathitkul [c,d,*]

[a] Department of Physics, Faculty of Science, Thaksin University, Phatthalung 93210 Thailand
[b] Institute of Nanomaterials Research and Innovation for Energy (IN-RIE), Khon Kaen University, Khon Kaen 40002 Thailand
[c] Department of Physics, Faculty of Science, Walailak University, Nakhon Si Thammarat 80160 Thailand
[d] Thailand Center of Excellence in Physics, Ministry of Higher Education, Science, Research and Innovation, Bangkok 10400 Thailand

ARTICLE INFO

Article history:
Received 30 April 2021
Revised 7 July 2021
Accepted 27 October 2021
Available online 2 November 2021

Keywords:
Barium hexaferrite
Sol–gel auto-combustion
Ion substitution
Magnetization
Coercivity

ABSTRACT

The partial substitution by bismuth (Bi) is aimed to improve magnetic properties of barium hexaferrites from the sol–gel auto-combustion synthesis. The exceptionally high saturation magnetization of 99 emu/g is attributed to the substitution of Fe^{3+} in tetrahedral $4f_1$ sites by $Bi^{3+}$and the highly compact structure without impurity phase. On the other hand, the coercivity is reduced with increasing Bi substitution because the hexagonal particles grow larger and single magnetic domains become multi-domains. Similarly, the co-substitution by bismuth-copper (Bi-Cu) ions substantially enhances the particle size and hence the reduction in coercivity is even more drastic. The reduction in coercivity of barium hexaferrites with high magnetizations are desirable for microwave absorbing and data storage materials. The magnetizations of barium hexaferrites with either Bi or Bi-Cu substitutions follow the law of approach saturation. However, the saturation magnetization is significantly lower by the Bi-Cu substitutions into octahedral $4f_2$ sites and the presence of the secondary hematite phase.

1. Introduction

Numerous applications in data storage and high-frequency devices as well as the product development of microwave absorbers and commercial permanent magnets lead to the research on tailoring electromagnetic properties of the M-type barium ferrites ($BaFe_{12}O_{19}$) (Pullar, 2012; Houbi et al., 2021). Hard/soft magnetic composites consisting of barium ferrites have also attracted the interest of permanent magnet manufacturers (Thirupathy et al., 2020). Besides the microstructure, ferrite properties are inherently related to the exchange interaction between ions occupying the lattice sites. One pathway to increase the magnetization is by the partial substitution of Fe^{3+} with other cations to reduce the magnetic moments coupled in an opposite direction (Pullar, 2012). Spontaneous polarization may also arise from such ion substitutions leading to multiferroic properties (Thirupathy et al., 2020).

Several methods were employed to substitute Fe^{3+} in barium ferrites by different ions. The substitution by scandium (Sc) via the hydrothermal method regulated the size and, hence magnetic properties of barium ferrite nanodiscs (Hähsler et al., 2020). The solid-state reaction method successfully introduced Sc (Wang et al., 2018), titanium (Ti) (Behera and Ravi, 2019), and neodymium (Nd) (Widanarto et al., 2018) into barium ferrites. The substitution by copper (Cu) was also demonstrated via the solid-state mixed oxide route (Rafiq et al., 2018). The co-precipitation was used to synthesize barium ferrites with Cu substitutions (Vadivelan and Jaya, 2016) and modified electrical permittivity as well as ac conductivity by the cobalt (Co) substitution (Shehabi et al., 2020). The substitution by aluminum (Al) in $BaFe_{12-x}Al_xO_{19}$ for x = 0.0, 2.0, and 4.0 using high-energy milling changed particle size and magnetic properties and the reflection loss at microwave frequency was optimized in the case of x = 2.0 (Winatapura et al., 2019). The co-substitution by Mn and Ti was achieved by mechanical alloying (Yustanti et al., 2020; Manaf et al., 2017).

* Corresponding author at: Department of Physics, Faculty of Science, Walailak University, Nakhon Si Thammarat 80160 Thailand.
E-mail address: schitnar@mail.wu.ac.th (C. Sirisathitkul).
Peer review under responsibility of King Saud University.

Production and hosting by Elsevier

https://doi.org/10.1016/j.jksus.2021.101682
1018-3647/

The sol–gel method has been used to synthesize barium ferrites with substantial maximum energy products. The method is also effective in partial substitutions of barium hexaferrite by Cu (Asiri et al., 2018; Kumar et al., 2020), Al (Han et al., 2021); Zr-Ni (Zhang et al., 2020), Co-Sm (Faisal et al., 2018; Asghar et al., 2020), Co-Dy-La (Mohammed et al., 2019), Nd-Cd-In (Jasrotia et al., 2019), and Bi (Iqbal et al., 2020). Iqbal and co-workers reported that the Bi-substituted barium ferrite strongly absorbed microwave in a higher frequency regime (8.2–12.4 GHz) than that by spinel ferrites but their magnetizations were moderate below 60 emu/g (Iqbal et al., 2020). From the line broadening in MÖssbauer spectra, Winotai and co-workers concluded that saturation magnetization of $BaFe_{12-x}Bi_xO_{19}$ was reduced by the substitution of low concentration in the octahedral sites but increased by substituting Bi^{3+} in the tetrahedral sites (Winotai et al., 2000). In this work, the sol–gel auto-combustion is used to synthesize Bi-substituted barium hexaferrite with enhanced magnetization. The co-substitution of Bi-Cu is also explored. Their effects on magnetic properties are related to the variation in phase and morphology of ferrite products.

2. Materials and methods

Six barium ferrite samples including a pristine sample (A) were synthesized by the sol–gel auto-combustion technique. The $BaFe_{12-x}Bi_xO_{19}$ samples with x = 0.1 and 0.5 are respectively referred to as B and C. Samples coded D, E, and F are $Ba_{1-x}Fe_{12-x}Bi_xCu_xO_{19}$ with x = 0.1, 0.2, and 0.3 respectively. Bi and Bi-Cu ions were introduced by adding bismuth(III) nitrate pentahydrate ($Bi(NO_3)_3{\cdot}5H_2O$) and copper(II) nitrate trihydrate ($Cu(NO_3)_2{\cdot}3H_2O$) in the reaction between iron(III) nitrate nonahydrate ($Fe(NO_3)_3{\cdot}9H_2O$) and barium nitrate ($Ba(NO_3)_3$). The starting materials were dissolved in 30 mL of deionized water. Then, 1.441 g of citric acid was added to the solution and completely dissolved under constant stirring. Citric acid is a fuel in the gel combustion commonly used for barium ferrite syntheses (Mohammed et al., 2019; Jasrotia et al., 2019). The pH of the solution was adjusted to 7 by adding ammonium hydroxide (NH_4OH) solution (25%). After heating at 90 °C for 230 min, the solution turned into a viscous gel. The next heating step at 150 °C for 190 min enabled the gel combustion resulting in a brown product. The ground product was subsequently heated in a furnace at 450 °C for 2 h and at 1050 °C for 3 h with a heating rate of 4.5 °C/min.

Crystalline phases were examined by X-ray diffractometer (XRD, Philips X'PERT MPD) using 1.5406 Å Cu-k_α radiation. The diffraction was measured at varying angles (2θ) from 20° to 80° with a scan rate of 0.5°/min. The unit cell volume (V_{cell}) was calculated from;

$$V_{cell} = \frac{\sqrt{3}}{2}a^2c \quad (1)$$

where a and c are lattice parameters. The crystallite size (d) was determined from the full width at half maximum of the most intense peak (B) using the Scherrer formula;

$$d = \frac{0.89\lambda}{B\cos\theta} \quad (2)$$

where θ is the angle of Bragg diffraction and λ is the wavelength of K_α X-ray (1.5406 Å).

Morphologies of ferrite samples were examined by a scanning electron microscope (SEM, FEI Quanta 450 FEG) using the accelerating voltage of 10 kV. Before the imaging, the samples were coated with Pd-doped Au by sputtering. The particle size in SEM micrographs were analyzed by the ImageJ program and the size distributions were presented in histograms. Room temperature magnetic properties were characterized by a vibrating sample magnetometer (VSM, VersaLab Quantum Design). To complete each hysteresis loop, the magnetic field was swept from –20 kOe to +20 kOe. The coercivity and remanence were respectively determined from the x- and y- intercept of the hysteresis loop.

3. Results and discussion

The XRD pattern of the pristine sample A in Fig. 1(a) exhibits characteristic peaks of barium hexaferrites with the magnetoplumbite structure (JCPDS: 43-0002). Diffractions from the (1 1 4) and (1 0 7) give rise to sharp peaks of high intensity. Besides, the trace of hematite (α-Fe_2O_3, JCPDS: 24-0081) is present as the second phase. Also shown in Fig. 1(a), the Bi substitution of x = 0.1 (sample B) gives rise to comparable barium hexaferrite peaks but the intensity of the hematite peak is reduced. The secondary hematite phase entirely disappears as x is increased to 0.5 (sample C). The effect of this Bi substitution is similar to the Cu substitution in enhancing the sintering and suppressing iron oxide formation (Rafiq et al., 2018). By contrast, the simultaneous substitutions by Bi and Cu in $Ba_{1-x}Fe_{12-x}Bi_xCu_xO_{19}$ exhibits the opposite effect on the secondary phase formation. As shown in Fig. 1(b), the intensity of the hematite phase is increased with increasing x from 0.1

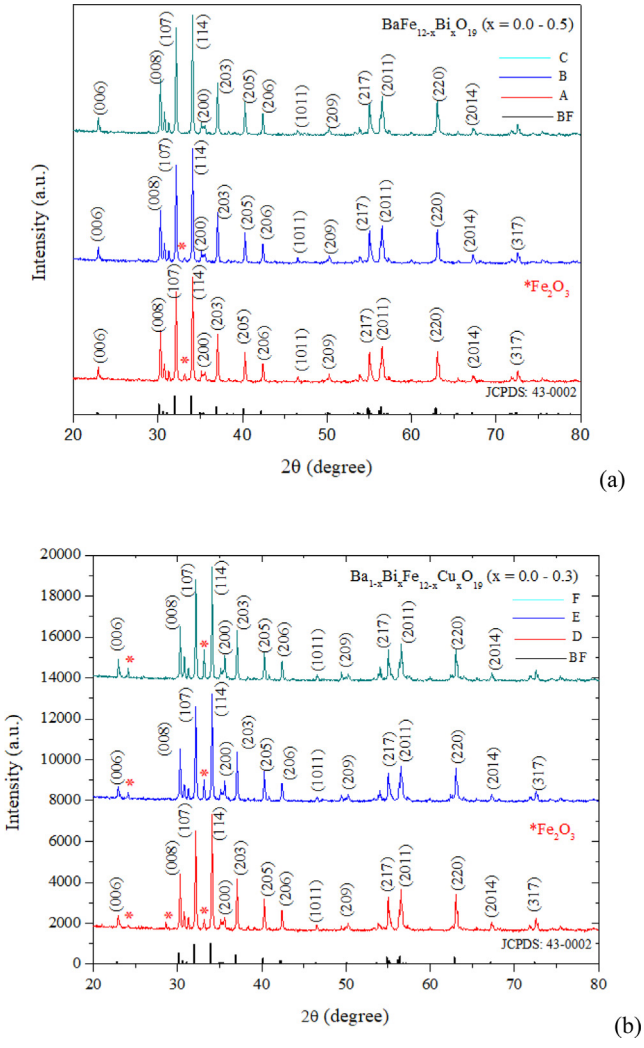

Fig. 1. XRD patterns of (a) $BaFe_{12-x}Bi_xO_{19}$ (A (x = 0), B (x = 0.1), C (x = 0.5)) and (b) $Ba_{1-x}Fe_{12-x}Bi_xCu_xO_{19}$ (D (x = 0.1), E (x = 0.2), F (x = 0.3)) samples compared to the barium hexaferrite standard.

to 0.3. The presence of hematite is a result of competing reaction which is not only dependent on the substitution but also the fuel used in the sol–gel auto-combustion (Sankaranarayanan and Khan, 1996; Godara et al., 2021). For the charge neutrality, the hematite formation can be increased with increasing ion substitutions (Katlakunta et al., 2015).

As listed in Table 1, the lattice parameter *a* is increased by only 0.034 % with the Bi substitution whereas the *c* value is decreased by 0.17% with the highest Bi-Cu co-substitution (sample F, x = 0.3). The *c*/*a* ratio does not significantly vary with the substitution and remains around 3.94. The value of less than 3.98 is consistent with the M-type hexaferrites (Chawla et al., 2014). The V_{cell} is expanded by only 0.029% by and reduced from 700.6 to 699.1 Å^3 only by the Bi-Cu co-substitution. The crystallite size of the pristine sample A is 63.88 nm and significantly rise with the increasing Bi substitution. However, the co-substitution of Bi and Cu does not monotonically increase the crystallite size and the reduction to 62.92 nm is observed in the case of sample E (x = 0.2). The irregular changing crystallite size was also observed in the case of co-substitution by Co-Zr ions with smaller average sizes (Chawla et al., 2014; Mudsainiyan et al., 2014).

The effect of Bi substitution on the morphology of barium hexaferrite is notable in Fig. 2. Similar to previous reports (Faisal et al., 2018; Asghar et al., 2020; Mohammed et al., 2019; Jasrotia et al., 2019), the agglomeration by magnetic interaction leads to the particle size much larger than the crystallite size. Also in Fig. 2, the particle size distributions are shown by histograms in the insets. The pristine sample is composed of irregular submicron particles with rough morphology. With increasing Bi substitution, the particles evolve into microscale with flat hexagonal facets reflecting the magnetoplumbite structure. The distinctive feature in the case of the highest Bi substitution x = 0.5 (sample C) is a highly compact stacking of microparticles. The particle growth is consistent with the increase in crystallite size of Bi-substituted barium ferrites. The size of hexagonal particles is even larger by the Bi-Cu substitutions. The trend is consistent with the barium hexaferrites substituted by Cu (Rafiq et al., 2018; Vadivelan and Jaya, 2016) and Ti (Behera and Ravi, 2019). In addition to ion substitutions, the sintering is clearly promoted.

The Bi and Bi-Cu substitutions influence magnetic properties as respectively shown by hysteresis loops in Fig. 3(a) and (b). Magnetic parameters deduced from these hysteresis loops are compared in Table 1. The coercivity (H_c in Table 1) is decreased with increasing Bi substitution similar to a previous report on the Cu substitution (Asiri et al., 2018). The Fe^{3+} ions in the 12k, $4f_2$, and 2b sites predominantly contribute to the magnetocrystalline anisotropy. Because the ion substitution does not drastically affect the *c*/*a* ratio, the coercivity change is not due to the anisotropy. Instead, such reduction is related to the increase in particle size observed in Fig. 2. The multi-domain structure, following the increase in particle size, requires a smaller magnetic field to switch its magnetization direction. It is also consistent with the larger particle size that the Bi-Cu substituted barium hexaferrites exhibit even lower values of coercivity. Such a trend was also observed by the co-substitution by Bi-Ti (Belous et al., 2006). The reduction in coercivity of barium hexaferrites with high magnetizations could be exploited in producing microwave absorbing and data storage materials. The remanence (M_r in Table 1) is also decreased from 34 to 27 emu/g with increasing Bi-Cu from x = 0.1 to 0.3. On the other hand, the increase in Bi substitution from 0.1 to 0.5 slightly affects the remanence of $BaFe_{12-x}Bi_xO_{19}$.

By increasing an applied magnetic field in the VSM measurement from 10 kOe in Fig. 3 to the maximum of 20 kOe, the hysteresis loops are still not saturated. The saturation magnetization (M_s in Table 1) is then approximated from the law of approach saturation. Magnetizations of hard ferrites approach the saturation value according to Eq. (3) (Bate, 1991).

$$M = M_s\left[1 - \frac{B}{H^2}\right] \tag{3}$$

where *B* is a constant. Eq. (3) can be written in a linear form in Eq. (4).

$$M = (-M_s B)\cdot\frac{1}{H^2} + M_s \tag{4}$$

In Fig. 4, the *M* values from the hysteresis loops in Fig. 3 are plotted against $1/H^2$. The linear trends are obtained in the case of Bi substitution with R^2 around 0.987–0.988. For Bi-Cu substitution, the R^2 is increased to 0.993–0.995 corresponding to lower magnetizations. The saturation magnetization, determined from the y-intercept in the plot of *M* against $1/H^2$, is 85 emu/g in the case of the pristine sample A. This saturation magnetization is much larger than typical values in the range of 42–63 emu/g (Chawla et al., 2014; Mudsainiyan et al., 2014), but comparable to those in some previous reports (Rafiq et al., 2018; Winatapura et al., 2019). In barium hexaferrites, Fe^{3+} ions in the 12k, 2a and 2b sites have their magnetic moments in parallel to the crystallographic *c*-axis, but those occupying the tetrahedral $4f_1$ and octahedral $4f_2$ sites are antiparallel. A higher occupancy of Fe^{3+} ions in the 12k sites lead to a larger magnetization (Rane et al., 2013).

The saturation magnetization is even higher by the Bi substitution and the maximum value of 99 emu/g obtained in sample C (x = 0.5) is likely due to the high packing density and purity of barium hexaferrite. Magnetic properties are changed as a result of partial substitutions in five sublattices of barium hexaferrites by di-, tri- and tetravalent ions (Chawla et al., 2014; Mudsainiyan et al., 2014; Vinnik et al., 2015). The increase in saturation magnetization is due to the substitution of Fe^{3+} in the tetrahedral $4f_1$ site by Bi^{3+}. Consistent with increasing hematite formations by the Bi-Cu addition, the increases of x to 0.2 and 0.3 in $Ba_{1-x}Fe_{12-x}Bi_xCu_xO_{19}$ yield

Table 1
Structural parameters from XRD and magnetic parameters from VSM of $BaFe_{12-x}Bi_xO_{19}$ and $Ba_{1-x}Fe_{12-x}Bi_xCu_xO_{19}$ samples.

	Structural parameter					Magnetic parameter			
Sample	a (Å)	c (Å)	c/a	V_{cell} (Å^3)	*d* (nm)	H_c (Oe)	M_r (emu/g)	M_s (emu/g)	M_r/M_s
$BaFe_{12-x}Bi_xO_{19}$									
A (x = 0.0)	5.899	23.25	3.942	700.6	63.88	1600	38	85	0.45
B (x = 0.1)	5.899	23.25	3.941	700.7	66.55	1593	43	97	0.44
C (x = 0.5)	5.901	23.24	3.939	700.8	69.88	1136	42	99	0.42
–	–	–	–	–	–	–	–	–	–
$Ba_{1-x}Fe_{12-x}Bi_xCu_xO_{19}$									
D (x = 0.1)	5.898	23.23	3.939	700.0	67.28	676	34	97	0.35
E (x = 0.2)	5.898	23.24	3.940	700.0	62.92	672	30	86	0.35
F (x = 0.3)	5.897	23.21	3.937	699.1	66.54	564	27	84	0.32

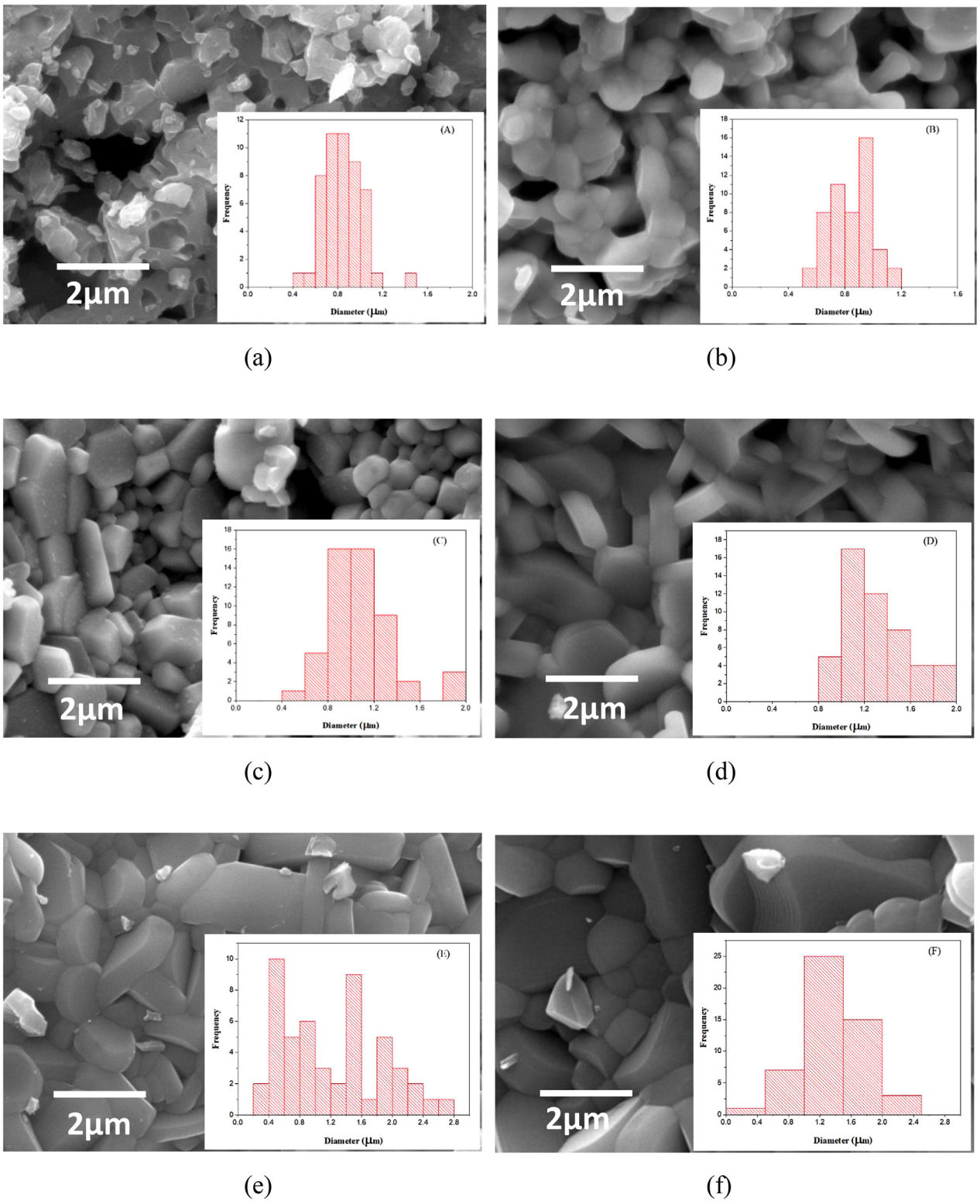

Fig. 2. Morphology of $BaFe_{12-x}Bi_xO_{19}$ ((a) sample A (x = 0), (b) sample B (x = 0.1), (c) sample C (x = 0.5)) and $Ba_{1-x}Fe_{12-x}Bi_xCu_xO_{19}$ ((d) sample D (x = 0.1), (e) sample E (x = 0.2), (f) sample F (x = 0.3)) imaged by SEM. Histograms of particle size distribution are shown in the insets.

lower saturation magnetizations than 97 emu/g by the lowest substitution of x = 0.1 (sample D). Besides the effect of phase impurity, the saturation magnetization is increased if cations substitute the Fe^{3+} in the tetrahedral sites. The magnetization in the case of substitution by Bi-Cu is likely reduced because the Fe^{3+} substitutions in the crystals can also occur at other sites depending on the type and concentration of ions (Belous et al., 2006). The ionic radii of Fe^{3+} in octahedral coordination (0.67 Å) and Cu^{2+} (0.78 Å) ions are comparable and Cu^{2+} tends to occupy the octahedral $4f_2$ site (Vinnik et al., 2015). The substitutions in octahedral sites tend to weaken exchange interactions of Fe^{3+}-O^{2-}-Fe^{3+} and therefore reduce the magnetization (Jasrotia et al., 2019; Godara et al.,

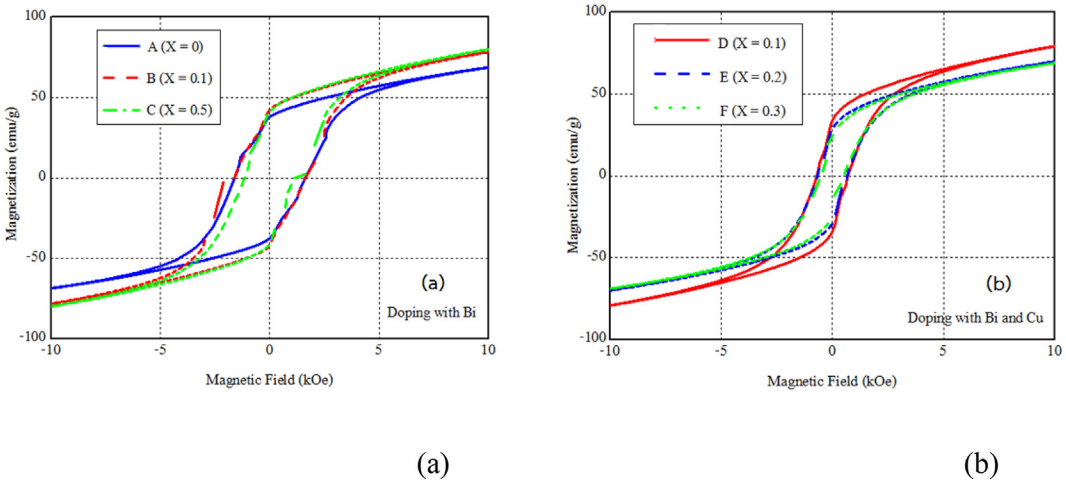

Fig. 3. Magnetic hysteresis loops of (a) $BaFe_{12-x}Bi_xO_{19}$ and (b) $Ba_{1-x}Fe_{12-x}Bi_xCu_xO_{19}$ samples.

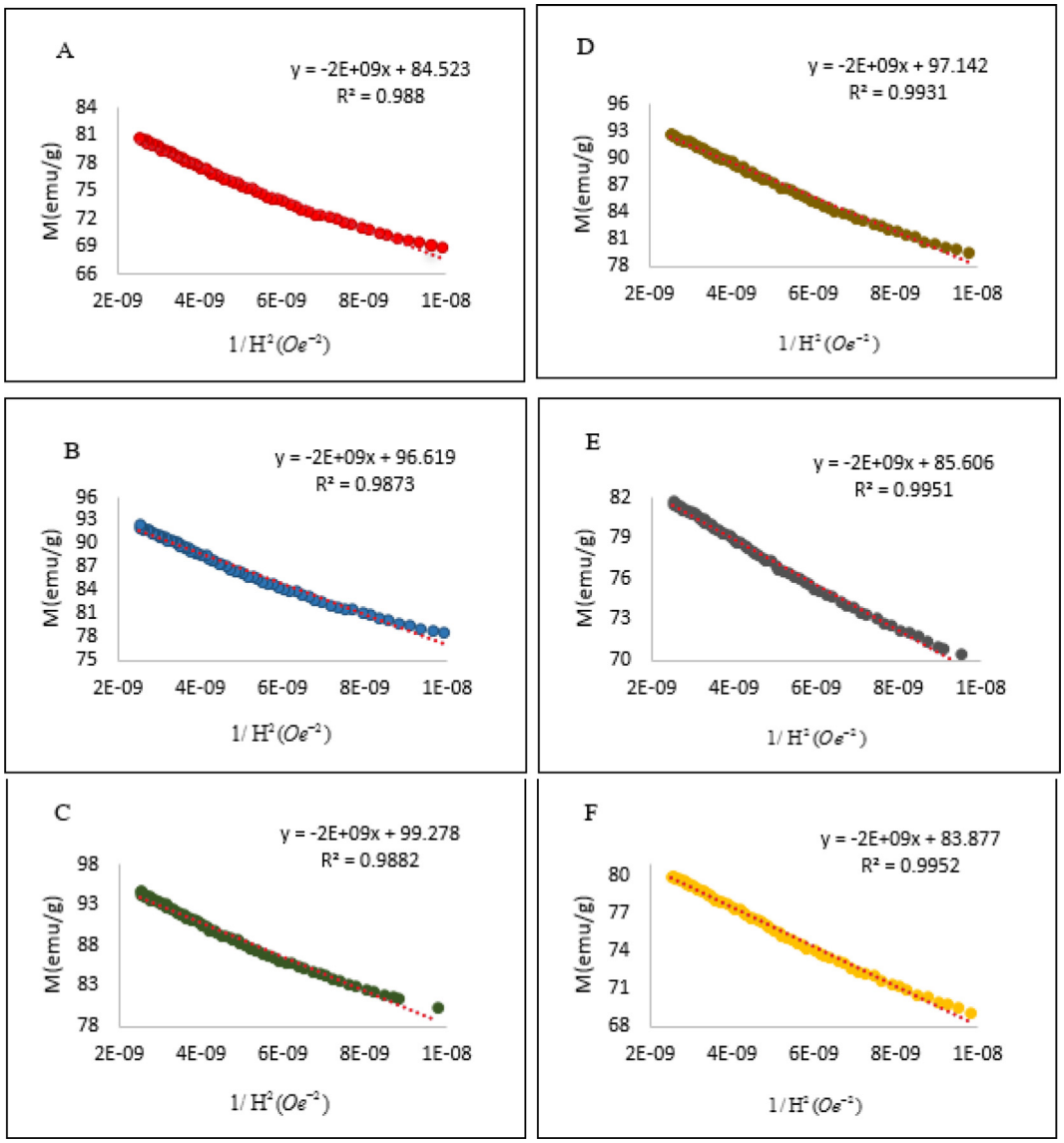

Fig. 4. Plots of M as a function of $1/H^2$ using the values from hysteresis loops of $BaFe_{12-x}Bi_xO_{19}$ (A (x = 0), B (x = 0.1), C (x = 0.5)) and $Ba_{1-x}Fe_{12-x}Bi_xCu_xO_{19}$ (D (x = 0.1), E (x = 0.2), F (x = 0.3)) samples.

2021). The ionic radii of Bi^{3+} (1.1 Å) are larger than those of Cu^{2+} and Fe^{3+} and the partial substitution of Ba^{2+} whose ionic radii is 1.5 Å (Barsoum, 2020), cannot be ruled out.

Finally, the squareness ratio (M_r/M_s in Table 1) of all ferrites are compared. The highest value of 0.45 is observed in the pristine sample, also with the highest coercivity, is attributed to particles with a single magnetic domain. The Bi substitution reduces the squareness ratio of barium hexaferrite. The squareness ratio is further reduced to 0.32–0.35 by the Bi-Cu substitution indicating multi-domain structures (Chawla et al., 2014; Mudsainiyan et al., 2014; Kagdi et al., 2018). The results are consistent with the increase in particle size and the reduction in coercivity. Interestingly, the values of squareness ratio over 0.6 were reported in co-substituted $BaFe_{12}O_{19}$ (Belous et al., 2006) and $BaFe_{12}O_{19}$/$CaCu_3Ti_4O_{12}$ composites (Mohammed et al., 2019).

4. Conclusions

The substitution of Bi in sol–gel derived $BaFe_{12-x}Bi_xO_{19}$ increased the size of hexagonal particles and the substitution of x = 0.5 inhibited the hematite formation as the second phase. Such an increase in particle size reduced the coercivity whereas the remanence remained rather constant. Interestingly, the saturation magnetization consistent with the law of approach saturation was as high as 99 emu/g in the case of x = 0.5. The particle size of $Ba_{1-x}Fe_{12-x}Bi_xCu_xO_{19}$ is even more enhanced by the substitution by Bi-Cu and it follows that the coercivity was decreased below 700 Oe. The magnetizations were also reduced by the high substitution by Bi-Cu.

Declaration of Competing Interest

The authors declare that they have no known competing financial interests or personal relationships that could have appeared to influence the work reported in this paper.

Acknowledgments

A scholarship was granted to the second author by Thailand Center of Excellence in Physics, Ministry of Higher Education, Science, Research and Innovation (Grant No. ThEP-63-PIP-WU3). This research was partially supported by the New Strategic Research (P2P) project, Walailak University, Thailand.

References

Asghar, G., Asri, S., Khusro, S.N., Tariq, G.H., Awan, M.S., Irshad, M., Safeen, A., Iqbal, Y., Shah, W.H., 2020. Enhanced magnetic properties of barium hexaferrite. J. Electron. Mater. 49, 4318–4323.

Asiri, S., Güner, S., Demir, A., Yildiz, A., Manikandan, A., Baykal, A., 2018. Synthesis and magnetic characterization of Cu substituted barium hexaferrites. J. Inorg. Organomet. Polym. Mater. 28, 1065–1071.

Barsoum, M.W., 2020. Fundamentals of Ceramics. CRC Press, Boca Raton.

Bate, G., 1991. Magnetic recording materials since 1975. J. Magn. Magn. Mater. 100, 413–424.

Behera, P., Ravi, S., 2019. Influence of Ti-substitution on structural, magnetic and dielectric properties of M-Type barium hexaferrite. J. Electron. Mater. 48, 5062–5074.

Belous, A.G., V'yunov, O.I., Pashkova, E.V., Ivanitskii, V.P., Gavrilenko, O.N., 2006. Mossbauer study and magnetic properties of M-type barium hexaferrite doped with Co+Ti and Bi+Ti ions. J. Phys. Chem. B 110, 26477–26481.

Chawla, S.K., Mudsainiyan, R.K., Meena, S.S., Yusuf, S.M., 2014. Sol–gel synthesis, structural and magnetic properties of nanoscale M-type barium hexaferrites $BaCo_xZr_xFe_{(12-x)}O_{19}$. J. Magn. Magn. Mater. 350, 23–29.

Faisal, M., Saeed, A., Larik, F.A., Ghumro, S.A., Rasheed, S., Channar, P.A., 2018. WOWS sol–gel based synthesis and structural, morphological, electrical and magnetic characterization of Co-Sm doped M-type barium hexaferrite materials. J. Electron. Mater. 47 (12), 7011–7022.

Godara, S.K., Dhaka, R.K., Kaur, N., Malhi, P.S., Kaur, V., Sood, A.K., Bahel, S., Bhadu, G. R., Chaudhari, J.C., Pushkarna, I., Singh, M., 2021. Synthesis and characterization of Jamun pulp based M-type barium hexaferrite via sol–gel auto-combustion. Results Phys. 22, 103903.

Godara, S.K., Kaur, V., Chuchra, K., Narang, S.B., Singh, G., Singh, M., Chawla, A., Verma, S., Bhadu, G.R., Chaudhari, J.C., Babu, P.D., Sood, A.K., 2021. Impact of Zn^{2+}-Zr^{4+} substitution on M-type barium strontium hexaferrite's structural, surface morphology, dielectric and magnetic properties. Results Phys. 22, 103892.

Hähsler, M., Zimmermann, M., Heißler, S., Behrens, S., 2020. Sc-doped barium hexaferrite nanodiscs: Tuning morphology and magnetic properties. J. Magn. Magn. Mater. 500, 166349.

Han, G., Sui, R., Yu, Y., Wang, L., Li, M., Li, J., Liu, H., Yang, W., 2021. Structure and magnetic properties of the porous Al-substituted barium hexaferrites. J. Magn. Magn. Mater. 528, 167824.

Houbi, A., Aldashevich, Z.A., Atassi, Y., Telmanovna, Z.B., Saule, M., Kubanych, K., 2021. Microwave absorbing properties of ferrites and their composites: A review. J. Magn. Magn. Mater. 529, 167839.

Iqbal, S., Khatoon, H., Kotnala, R.K., Ahmad, S., 2020. Bi-doped barium ferrite decorated polythiophene nanocomposite: influence of Bi-doping on structure, morphology, thermal and EMI shielding behavior for Xband. J. Mater. Sci. 55, 15894–15907.

Jasrotia, R., Singh, V.P., Kumar, R., Singh, K., Chandel, M., Singh, M., 2019. Analysis of Cd^{2+} and In^{3+} ions doping on microstructure, optical, magnetic and Mossbauer spectral properties of sol-gel synthesized BaM hexagonal ferrite based nanomaterials. Results Phys. 12, 1933–1941.

Kagdi, A.R., Solanki, N.P., Carvalho, F.E., Meena, S.S., Bhatt, P., Pullar, R.C., Jotania, R. B., 2018. Influence of Mg substitution on structural, magnetic and dielectric properties of X-type barium zinc hexaferrites $Ba_2Zn_{2-x}Mg_xFe_{28}O_{46}$. J. Alloys Compd. 741, 377–391.

Katlakunta, S., Meena, S.S., Srinath, S., Bououdina, M., Sandhya, R., Praveena, K., 2015. Improved magnetic properties of Cr^{3+} doped $SrFe_{12}O_{19}$ synthesized via microwave hydrothermal route. Mater. Res. Bull. 63, 58–66.

Kumar, S., Guha, S., Supriya, S., Pradhan, L.K., Kar, M., 2020. Correlation between crystal structure parameters with magnetic and dielectric parameters of Cu-doped barium hexaferrite. J. Magn. Magn. Mater. 499, 166213.

Manaf, A., Hafizah, M.A.E., Nainggolan, B.B., Manawan, M.T.E., 2017. Magnetic and microwave absorption characteristics of Ti^{2+}- Mn^{4+} substituted barium hexaferrite. Int. J. Technol. 8, 458–465.

Mohammed, J., Carol, T.T., Hafeez, H.Y., Basandraia, D., Bhadu, G.R., Godara, S.K., Narang, B., Srivastava, A.K., 2019. Electromagnetic interference (EMI) shielding, microwave absorption, and optical sensing properties of BaM/CCTO composites in Ku-band. Results Phys. 13, 102307.

Mudsainiyan, R.K., Chawla, S.K., Meena, S.S., 2014. Correlation between site preference and magnetic properties of Co–Zr doped $BaCo_xZr_xFe_{(12-2x)}O_{19}$ prepared under sol–gel and citrate precursor sol–gel conditions. J. Alloys Compd. 615, 875–881.

Pullar, R.C., 2012. Hexagonal ferrites: A review of the synthesis, properties and applications of hexaferrite ceramics. Prog. Mater. Sci. 57 (7), 1191–1334.

Rafiq, M.A., Waqar, M., Muhammad, Q.K., Waleed, M., Saleem, M., Anwar, M.S., 2018. Conduction mechanism and magnetic behavior of Cu doped barium hexaferrite ceramics. J. Mater. Sci.: Mater Electron. 29, 5134–5142.

Rane, V.A., Meena, S.S., Gokhale, S.P., Yusuf, S.M., Phatak, G.J., Date, S.K., 2013. Synthesis of low coercive $BaFe_{12}O_{19}$ hexaferrite for microwave applications in low-temperature cofired ceramic. J. Electron. Mater. 42, 761–768.

Sankaranarayanan, V., Khan, D., 1996. Mechanism of the formation of nanoscale M-type barium hexaferrite in the citrate precursor method. J. Magn. Magn. Mater. 153, 337–346.

Shehabi, H., Rekaby, M., Hassan, R.S., Awad, R., 2020. Microstructure and dielectric properties of $BaFe_{12}O_{19}$ hexaferrite nanoparticles: effect of cobalt addition and calcination temperature. Jordan J. Phys. 13, 211–219.

Thirupathy, C., Lims, S.C., Sundaram, S.J., Mahmoud, A.H., Kaviyarasu, K., 2020. Equilibrium synthesis and magnetic properties of $BaFe_{12}O_{19}$/$NiFe_2O_4$ nanocomposite prepared by co- precipitation method. J. King Saud Univ. Sci. 32, 1612–1618.

Vadivelan, S., Jaya, N.V., 2016. Investigation of magnetic and structural properties of copper substituted barium ferrite powder particles via co-precipitation method. Results Phys. 6, 843–850.

Vinnik, D.A., Tarasova, A.Y., Zherebtsov, D.A., Mashkovtseva, L.S., Gudkova, S.A., Nemrava, S., Yakushechkina, A.K., Semisalova, A.S., Isaenko, L.I., Niewa, R., 2015. Cu-substituted barium hexaferrite crystal growth and characterization. Ceram. Int. 41, 9172–9176.

Wang, Y., Liu, Y., Zhang, H., Li, J., Gao, L., Chen, D., Chen, Y., 2018. Preparation of scandium-doped, textured, M-type barium ferrite via a wet magnetizing orientation process. J. Electron. Mater. 47, 1330–1334.

Widanarto, W., Ardenti, E., Ghoshal, S.K., Kurniawan, C., Effendi, M., Cahyanto, W.T., 2018. Significant reduction of saturation magnetization and microwave-reflection loss in barium-natural ferrite via Nd^{3+} substitution. J. Magn. Magn. Mater. 456, 288–291.

Winatapura, D.S., Deswita, Fisli, A., Adi, W.A., 2019. Mechanosynthesis, crystal structure, magnetic and absorption properties of Al substituted $BaFe_{12}O_{19}$. J. Teknol. 81, 179–184.

Winotai, P., Thongmee, S., Tang, I.M., 2000. Cation distribution in bismuth-doped M-type barium hexaferrite. Mater. Res. Bull. 35, 1747.

Yustanti, E., Trenggono, A., Manaf, A., 2020. Physical and microwave absorption characteristics of high powered ultrasonically irradiated crystalline $BaFe_9Mn_{1.5}Ti_{1.5}O_{19}$ particles. Int. J. Technol. 11, 310–321.

Zhang, Y., Liu, C., Zhao, X., Yao, M., Miao, X., Xu, F., 2020. Enhanced microwave absorption properties of barium ferrites by Zr^{4+}-Ni^{2+} doping and oxygen-deficient sintering. J. Magn. Magn. Mater. 494, 165828.